



## Structural and optical analyses of GaP/Si and (GaAsPN/GaPN)/GaP/Si nanolayers for integrated photonics on silicon

Thanh Tra Nguyen, Cédric Robert Robert, Weiming Guo, Antoine Létoublon, Charles Cornet, Georges Elias, Anne Ponchet, Tony Rohel, Nicolas Bertru, Andrea Balocchi, et al.

### ► To cite this version:

Thanh Tra Nguyen, Cédric Robert Robert, Weiming Guo, Antoine Létoublon, Charles Cornet, et al.. Structural and optical analyses of GaP/Si and (GaAsPN/GaPN)/GaP/Si nanolayers for integrated photonics on silicon. *Journal of Applied Physics*, 2012, 112 (5), pp.053521. 10.1063/1.4751024 . hal-00726722

**HAL Id: hal-00726722**

**<https://hal.science/hal-00726722>**

Submitted on 23 Apr 2018

**HAL** is a multi-disciplinary open access archive for the deposit and dissemination of scientific research documents, whether they are published or not. The documents may come from teaching and research institutions in France or abroad, or from public or private research centers.

L'archive ouverte pluridisciplinaire **HAL**, est destinée au dépôt et à la diffusion de documents scientifiques de niveau recherche, publiés ou non, émanant des établissements d'enseignement et de recherche français ou étrangers, des laboratoires publics ou privés.

## Structural and optical analyses of GaP/Si and (GaAsPN/GaPN)/GaP/Si nanolayers for integrated photonics on silicon

T. Nguyen Thanh, C. Robert, W. Guo, A. Létoublon, C. Cornet, G. Elias, A. Ponchet, T. Rohel, N. Bertru, A. Balocchi, O. Durand, J. S. Micha, M. Perrin, S. Loualiche, X. Marie, and A. Le Corre

Citation: *Journal of Applied Physics* **112**, 053521 (2012); doi: 10.1063/1.4751024

View online: <https://doi.org/10.1063/1.4751024>

View Table of Contents: <http://aip.scitation.org/toc/jap/112/5>

Published by the [American Institute of Physics](#)

---

### Articles you may be interested in

[Control and elimination of nucleation-related defects in GaP/Si\(001\) heteroepitaxy](#)

*Applied Physics Letters* **94**, 232106 (2009); 10.1063/1.3154548

[Nucleation-related defect-free GaP/Si\(100\) heteroepitaxy via metal-organic chemical vapor deposition](#)

*Applied Physics Letters* **102**, 142102 (2013); 10.1063/1.4801498

[Laser operation of Ga\(NAsP\) lattice-matched to \(001\) silicon substrate](#)

*Applied Physics Letters* **99**, 071109 (2011); 10.1063/1.3624927

[Evaluation of InGaPN and GaAsPN materials lattice-matched to Si for multi-junction solar cells](#)

*Journal of Applied Physics* **113**, 123509 (2013); 10.1063/1.4798363

[InGaAs/GaP quantum dot light-emitting diodes on Si](#)

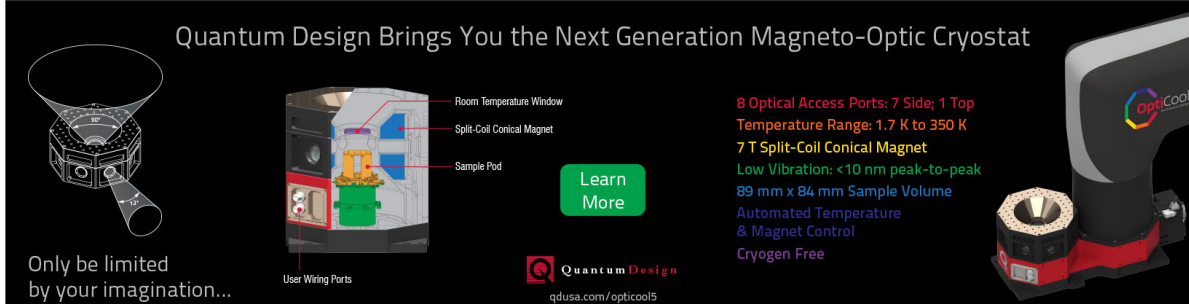
*Applied Physics Letters* **103**, 141906 (2013); 10.1063/1.4824029

[Band gaps of GaPN and GaAsN alloys](#)

*Applied Physics Letters* **70**, 3558 (1997); 10.1063/1.119232

---

Quantum Design Brings You the Next Generation Magneto-Optic Cryostat



Only be limited by your imagination...

Room Temperature Window  
Split-Coil Conical Magnet  
Sample Pod  
User Wiring Ports

[Learn More](#)

Quantum Design  
qdusa.com/opticool5

8 Optical Access Ports: 7 Side; 1 Top  
Temperature Range: 1.7 K to 350 K  
7 T Split-Coil Conical Magnet  
Low Vibration: <10 nm peak-to-peak  
89 mm x 84 mm Sample Volume  
Automated Temperature & Magnet Control  
Cryogen Free

OptiCool

# Structural and optical analyses of GaP/Si and (GaAsPN/GaPN)/GaP/Si nanolayers for integrated photonics on silicon

T. Nguyen Thanh,<sup>1,a)</sup> C. Robert,<sup>1</sup> W. Guo,<sup>1</sup> A. Létoublon,<sup>1</sup> C. Cornet,<sup>1</sup> G. Elias,<sup>2</sup> A. Ponchet,<sup>2</sup> T. Rohel,<sup>1</sup> N. Bertru,<sup>1</sup> A. Balocchi,<sup>3</sup> O. Durand,<sup>1</sup> J. S. Micha,<sup>4</sup> M. Perrin,<sup>1</sup> S. Loualiche,<sup>1</sup> X. Marie,<sup>3</sup> and A. Le Corre<sup>1</sup>

<sup>1</sup>Université Européenne de Bretagne, INSA, FOTON-OHM, UMR 6082, F-35708 RENNES, France

<sup>2</sup>CEMES, CNRS UPR 8011 et Université de Toulouse, 29 rue Jeanne Marvig, 31055 Toulouse, France

<sup>3</sup>Université de Toulouse, INSA-CNRS-UPS, LPCNO, 135 avenue de Rangueil, 31077 Toulouse, France

<sup>4</sup>UMR SPrAM 5819 CNRS-CEA-UJF, INAC, F-38054 Grenoble, France

(Received 22 June 2012; accepted 9 August 2012; published online 12 September 2012; publisher error corrected 14 September 2012)

We report a structural study of molecular beam epitaxy-grown lattice-matched GaP/Si(0 0 1) thin layers with an emphasis on the interfacial structural properties, and optical studies of GaAsP(N)/GaP(N) quantum wells coherently grown onto the GaP/Si pseudo substrates, through a complementary set of characterization tools. Room temperature photoluminescence at 780 nm from the (GaAsPN/GaPN) quantum wells grown onto a silicon substrate is reported. Despite this good property, the time-resolved photoluminescence measurements demonstrate a clear influence of non-radiative defects initiated at the GaP/Si interface. It is shown from simulations, how x-ray diffraction can be used efficiently for analysis of antiphase domains. Then, qualitative and quantitative analyses of antiphase domains, micro-twins, and stacking faults are reported using complementarity of the local transmission electron microscopy and the statistical x-ray diffraction approaches. © 2012 American Institute of Physics. [<http://dx.doi.org/10.1063/1.4751024>]

## I. INTRODUCTION

In the context of the monolithic integration of photonics on silicon, quasi-lattice-matched GaP (III-V semiconductor) epitaxially grown on Si has been proposed to overcome the well-known issue of the lattice mismatch, inherent to the growth of most III-V materials onto silicon substrates.<sup>1–6</sup> This opens the route for the coherent growth of a direct bandgap material on GaP-Si pseudo-substrates, using, for instance, diluted-nitrides GaPN-based materials. These materials are known to develop suitable optical properties<sup>7–9</sup> which will enable the elaboration of III-V laser diodes onto silicon, being a highly rewarding route to the fabrication of chip-to-chip and on-chip interconnects. Up to now, the GaAsPN materials system has reached the best performances for laser devices development on silicon, even if the effect of nitrogen on device properties and carrier life-time has not been clarified yet.<sup>10</sup> Such heterostructure development is also driven by the elaboration of high performance multi-junction solar cells onto the low-cost Si substrate.<sup>11</sup>

Long-term stable device performance implies reproducible achievement of defect-free interfaces between the III-V material and the Si substrate. Beyond the well-known related lattice mismatch defects (dislocations), other types of defects can be generated at the GaP/Si interface: among them antiphase domains (APD), which may develop in the case of polar on a non-polar crystal growth,<sup>1</sup> and microtwins (MT) are quite difficult to avoid.<sup>12</sup> Their density and

their emergence at the GaP surface must be avoided for the subsequent growth of any active area as photoluminescence (PL) properties (carrier life-time) are directly linked to the defects density.<sup>13</sup> Therefore, reliable structural analyses techniques have been used in recent years in order to address the issue of the defect density lowering in the GaP/Si material system, in order to elaborate the GaP/Si pseudo-substrates suitable for the subsequent growth of laser, or solar cell, heterostructure. For instance, an *in situ* monitoring technique of the APD detection has been developed using reflectance anisotropy spectroscopy<sup>14,15</sup> while transmission electron microscopy (TEM) has more often been used for *ex situ* analysis of APD and other typical defects (see for instance Refs. 16, 17, and references therein). However, TEM requires sample preparation and a TEM image is less statistically representative.

Therefore, the present paper describes a study of the structural properties of thin GaP layers epitaxially grown onto Si(0 0 1) substrates, as a first route toward the elaboration of GaP/Si pseudo-substrates. X-ray diffraction (XRD) is presented as a suitable tool for fast, robust, and non-destructive techniques complementary to TEM analyses. To this end, XRD analyses laboratory set-up tools are proposed to provide rapid feedback for growth condition optimization toward the elimination of emerging defects such as antiphase domains, detrimental for the obtaining of a defect-free GaP surface suitable for the subsequent growth of a heterostructure. Moreover, deeper XRD analyses performed on both a laboratory setup and on synchrotron, combined with TEM, AFM, and time-resolved optical characterization performed on GaAsPN QWs very near the GaP/Si interface, are shown to produce a breadth of complementary information on the

<sup>a)</sup> Author to whom correspondence should be addressed. Electronic mail: thanh-tra.nguyen@insa-rennes.fr. Tel.: +33 2 2323 8305. Fax: +33 2 2323 8618.

defects in molecular beam epitaxy (MBE)-grown GaP thin films onto Si(0 0 1) misoriented substrates.

## II. EXPERIMENTS

### A. Samples growth

The 20 nm GaP layers have been grown by MBE using migration enhanced epitaxy (MEE) which consists in alternated growth of Ga and P atomic layers and aims to limit the density of planar defects originating from island-like nucleation.<sup>9,18</sup> The growth is performed on a (0 0 1) misoriented Si ( $4^\circ$ -off toward [1 1 0]) suitable for APD density limitation<sup>9,19,20</sup> after a chemical (modified RCA) cleaning process and thermal (10 min at  $900^\circ\text{C}$ ) treatment of the Si surface. Three samples have been elaborated for the study of defects originated from the GaP/Si interface. The growth temperature ( $T_g$ ) of the first 2 samples was set to  $450^\circ\text{C}$ . The second sample was annealed 10 min at  $600^\circ\text{C}$  after growth. We call from now on the samples S450 and S450a, respectively, for the samples grown at  $450^\circ\text{C}$  without and with post annealing. For the third sample (S350), the  $T_g$  was set at  $350^\circ\text{C}$  without post growth annealing. The GaP/Si is further used as a virtual substrate for the subsequent growth of active layers. A double GaAsPN/GaPN quantum well has been grown on this virtual substrate for the study of optical properties.<sup>21</sup> The active area is located at 160 nm away from the GaP/Si interface.

### B. Temperature dependent and time-resolved photoluminescence

PL experiments were carried-out exciting the samples with a 405 nm continuous wave laser diode. The power density is roughly estimated to  $80\text{ W cm}^{-2}$ . The samples were set in a Helium bath closed cycle cryostat to study PL from 10 K to room temperature (RT). For time resolved PL, the sample was excited at 405 nm by a frequency doubled Ti:Sapphire with a repetition rate of 80 MHz and the power density is estimated to  $4000\text{ W cm}^{-2}$ . The luminescence was detected by a synchroscan Hamamatsu streak camera with an overall time resolution of 8 ps and the measurements were performed at different temperatures.

### C. X-ray diffraction experiments

#### 1. Lab setup

XRD has been performed on the three samples (S450, S450a, S350) using the laboratory setup working at a wavelength of 0.15406 nm (Cu  $K\alpha_1$ ). The resolution function allows a good separation of the layer from the substrate contributions and the identification of short range correlation features up to about 300 nm on the (0 0 4) in the lateral direction (here parallel to [1 1 0]). XRD shows a highly coherent growth for the 3 samples (low plastic relaxation). A linear detector with 188 channels has been used. Placed 270 mm away from the sample it allows detection width of  $3^\circ$  in  $2\theta$ . This enables much faster reciprocal space map (RSM) measurements than with a traditional point detector.

### 2. Synchrotron XRD (ESRF)

Synchrotron XRD has been also employed in grazing incidence condition to enhance the contribution of the GaP layer. The experiment has been performed at 10 keV, which allows to avoid Ga fluorescence above K edge at 10.36 keV. This energy corresponds to a wavelength of 0.123984 nm. The incident angle has been fixed to  $0.2^\circ$ . The beam size was  $0.5 \times 0.5\text{ mm}^2$  at the goniometer center. 2 slit sets are placed on the detection arm, near the sample and 810 mm away. The slit opening was  $1 \times 1\text{ mm}^2$ .

### D. Transmission electron microscopy experiments

TEM has also been performed in plan-view and cross section geometries ([1  $\bar{1}$  0] zone axis) on the S350 and a different sample prepared in the same conditions than for the S350 with the addition of a GaAsP super lattice on top of the GaP thin layer. Thin plates have been prepared for these two samples by mechanical polishing and ion thinning. The experiment has been performed on a Philips CM30 in high resolution and conventional modes, with an acceleration voltage of 300 kV.

## III. RESULTS AND DISCUSSION

### A. Pseudomorphic growth of GaP/Si

Fig. 1 presents a RSM centred on the (0 0 4) reflection of the sample S450.  $S_x$  and  $S_z$  are the projection of the reciprocal space vector  $S$  ( $S = (2/\lambda) \sin(\theta)$ ) along the two directions X (coplanar both with the sample surface and the scattering plane) and Z perpendicular to the sample surface. This coordinate system clearly shows the offcut angle effect. In this case, (0 0  $l$ ) reflections are not strictly specular as they are for a (0 0 1) nominal substrate. The crystallographic direction [1 1 0] being coplanar with the scattering plane, the  $4^\circ$  offcut angle is not compensated by a tilt of  $\chi$  but by a  $4^\circ$  angle correction on  $\omega$  (here  $\omega = \theta - 4^\circ$ ).<sup>4</sup> On this graph, the

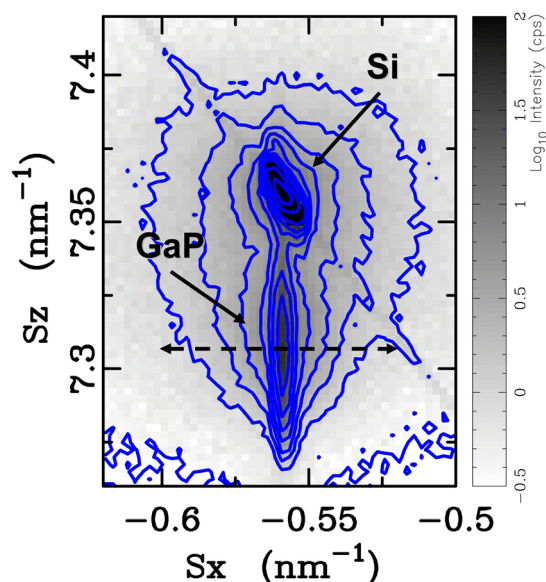


FIG. 1. RSM ( $\log_{10}$  intensity levels) around (0 0 4) showing both the Si and the GaP contributions. The dashed arrow shows the transverse scan path.



GaP peak shape is typical of a thin epitaxial layer coherently grown on vicinal Si substrate.<sup>4</sup>

Fig. 2 shows the high resolution transmission electron microscopy (HRTEM) image of the GaP/Si interface. On this image, the GaP/Si interface is shown to be coherent with, however, an interfacial dislocation (ED) on the right of the image. A large step bunching is also observed with a height difference of about 4 nm which is much higher than the targeted 2 Si monolayer step height. This huge step bunching is probably due to an unoptimized chemical and thermal preparation of the surface with the presence of impurities.

## B. Optical properties of the (GaAsPN/GaPN)/GaP/Si(001) QWs

Fig. 3 shows the continuous wave PL spectra measured at 17 K and 106 K on GaAsPN/GaPN/Si QWs (black solid line and blue dashed line, respectively). The peak at higher energy is the signal of GaPN barrier, and the other is the GaAsPN QW peak. Despite the GaP/Si interface proximity and its related defects, a clear PL signal of GaAsPN QW is detected up to 300 K with a wavelength of 780 nm (1.58 eV), as presented in Fig. 3 inset. Now looking at the time-resolved PL properties (see Fig. 4), the luminescence decay clearly shows a non-single exponential behaviour which is typical in disordered systems such as diluted nitride alloys.<sup>22</sup> Nevertheless, the curves can be satisfactorily described by a double exponential fit. At 10 K, the decay times are 140 ps and 1250 ps. At 300 K, these times are dramatically shortened to 30 ps and 180 ps, respectively. Given the room temperature PL intensity and the time-resolved PL results, and given the vicinity of the GaP/Si interface, the optical emission is likely due to efficient carrier injection in well-localised radiative centres at low temperature. These centres are separated by structural defects (non-radiative centers), thermally activated at higher temperature. This demonstrates the optical limitation of the structure (coming from the GaP/Si originating defects), but information is, however, lacking for any improvement of the GaP/Si growth. We have there-

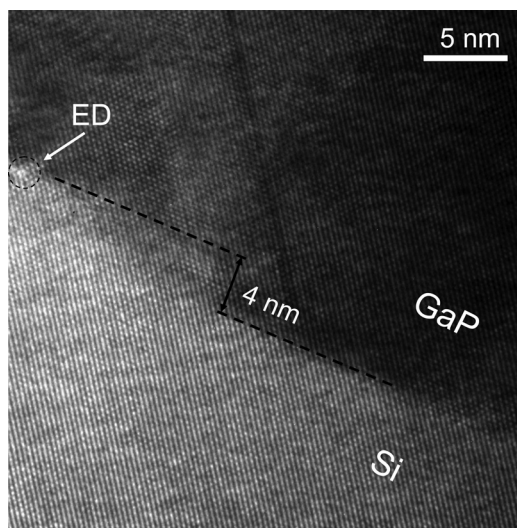


FIG. 2. HRTEM micrograph shows a coherent GaP/Si interface. An interfacial dislocation is identified (ED in the image).

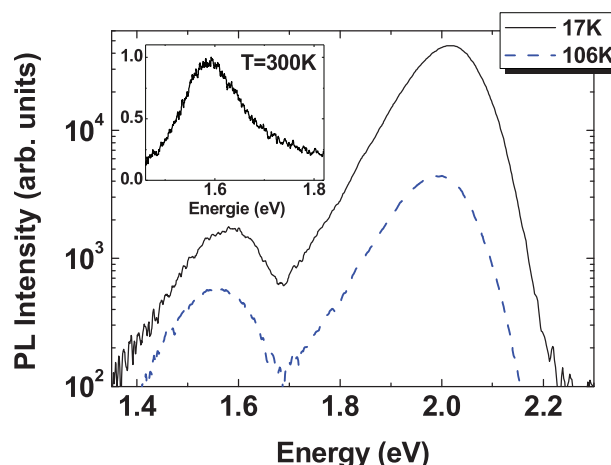


FIG. 3. Photoluminescence at 17 K and 106 K (black solid line and blue dashed line) of GaAsPN/GaPN quantum wells grown on Si substrate very near the GaP/Si interface. The inset shows the photoluminescence spectrum detected at 300 K.

fore developed a reliable method to characterize defects, using XRD-based technique.

## C. Antiphase domains analysis

### 1. Principle

APD characterization using XRD has been long ago presented (see also Ref. 17 for a review) and has been also applied in thin films for AlGaIn on sapphire,<sup>23</sup> GaAs on Si,<sup>24</sup> and GaP on Si.<sup>25,26</sup> The idea is that weak “antiphase” reflections (APR) act as APD sensors. Indeed Ga and P scatter in antiphase around weak reflections and in phase around strong reflections (SR). Ga and P positions are just exchanged in an APD when compared to the surrounding main phase matrix.<sup>27</sup> The APD does not break the lateral long range order given by epitaxy but gives a broad peak around antiphase reflections with a weaker peak maximum intensity. The broad peak profile is the characteristic of the APD width. This result can be explained by simple considerations on form and structure factors. When looking at scattered amplitude and intensity around Bragg reflections, all structure and

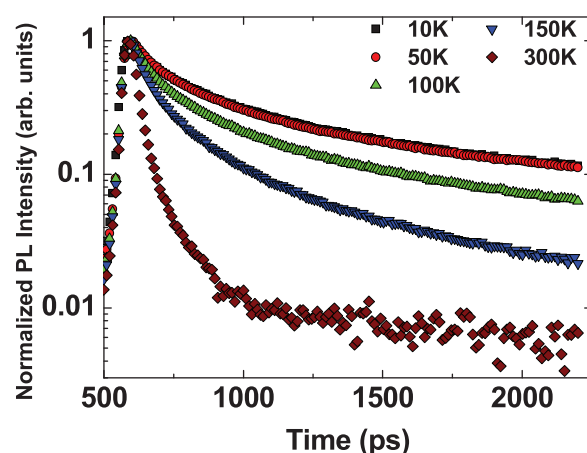


FIG. 4. Time-resolved photoluminescence spectra of GaAsPN/GaPN QWs near (160 nm) the GaP/Si interface. The detection energy corresponds to the peak of the spectrum for a given temperature.

form factors can be considered as real and can be added simply. Then, in the vicinity of a strong reflection ((0 0 4) for instance), the scattered amplitude is roughly proportional to

$$A_{Total}(S) \approx (F_{MP}(S) + F_{APD}(S)) \cdot F_{SR}(S). \quad (1)$$

We call  $F_{Total}(S)$  the form factor of the whole layer (main phase and APD) and  $F_{APD}(S)$  and  $F_{MP}(S)$  are, respectively, the APD and main phase form factors. The zinc-blend cell structure factor on strong reflections is  $F_{SR}(S) = 4 \cdot (f_{Ga}(S) + f_P(S))$  and the factor 4 is simplified to 1 hereafter.

Equation (1) rewrites

$$A_{Total}(S) \approx F_{Total}(S) \cdot F_{SR}(S), \quad (2)$$

since  $F_{MP}(S) + F_{APD}(S) = F_{Total}(S)$ . Similarly, for weak reflections ((0 0 2) and (0 0 6)), the scattered amplitude is roughly proportional to:  $A_{Total}(S) \approx (F_{MP}(S) - F_{APD}(S)) \cdot F_{APR}(S)$  where the zinc-blend cell structure factor is  $F_{APR}(S) = 4 \cdot (f_{Ga}(S) - f_P(S))$ . Indeed, because of Ga/P exchange and of  $f_{Ga}(S) - f_P(S)$  term, the cell structure factor takes an opposite value when going from the main phase to the APD. Equation (2) rewrites

$$A_{Total}(S) \approx (F_{Total}(S) - 2F_{APD}(S))F_{APR}(S). \quad (3)$$

Finally, from these equations, the scattered intensity around strong reflections is proportional to

$$|A_{Total}(S)|^2 \approx F_{Total}^2(S) \cdot (F_{SR}(S))^2 \quad (4)$$

and around weak reflections, it is proportional to

$$|A_{Total}|^2 \approx (F_{Total}^2 + 4F_{APD}^2 - 4F_{Total} \cdot F_{APD}) \cdot (F_{APR})^2. \quad (5)$$

The dependence with  $S$  is omitted for concision in the last equation.

These two equations (4) and (5) help to understand the following features: (1) APD brightly appears on APR with a factor 4 enhancement when compared to the contribution of a void of the same shape ( $4F_{APD}^2$  term in Eq. (5)); (2) APD contribution remains hidden on SR; (3) the long range lateral coherency (thin peak) remains even on APR (when APD density is not too large) with the term  $F_{Total}^2$ .

These features can be also illustrated by a simple simulation. In this simulation, a single APD with APB lying on the (1 1 0) planes, has been inserted in a GaP layer as presented in the Fig. 5(a) (left hand side). The intensity is calculated by using the Fourier transform of the whole structure. The scattered intensity simulation on transverse scans through (0 0 2) and (0 0 4) GaP reflections, along the [1 1 0] direction is presented on the right. The (0 0 4) transverse scan shows a very sharp peak of which the breadth corresponds to  $1/W_{Box}$ ,  $W_{Box}$  being the width of the simulation box in the [1 1 0] direction. The APD contribution shows up as the “broad component” in the (0 0 2). It has been also checked that the inter fringes distance gives the APD lateral size in the [1 1 0] direction:  $W_{APD} = 1/\Delta S$ . Fringes are generally not observed in real measurements. Moreover, different defects can contribute to the broad component of the Bragg

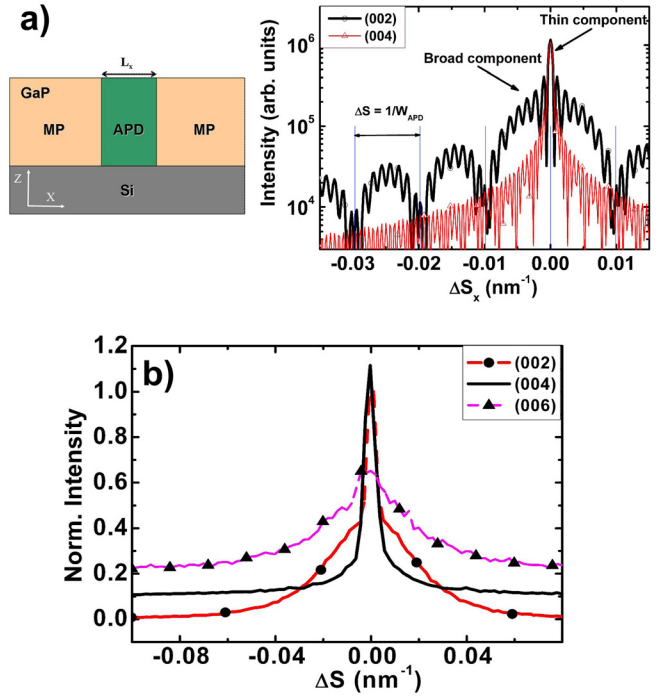


FIG. 5. (a) Simulation model of an APD with the lateral length  $L_x$  and (1 1 0) boundaries inserted in the main phase (MP) GaP layer on Si substrate (left) and transverse scan simulations through (0 0 2) and (0 0 4) GaP reflections (right). (b) XRD transverse scans on (0 0 2), (0 0 4), and (0 0 6) GaP reflection showing APD broadening of weak reflections for the sample S450a. The (0 0 2) and (0 0 4) scans have been normalized to the same maximum. The (0 0 6) scan has been normalized to (0 0 2) broad peak. The (0 0 4) and (0 0 6) scans have been shifted vertically for clarity.

peaks: micromosaicity, size effect (APD, microtwins, voids), strain, etc. Correlation lengths can be then deduced from integral widths of different peaks and Williamson-Hall like analysis can be employed for the identification of defects contributions.

## 2. XRD lab setup

Transverse scans are extracted from RSM on (0 0 2), (0 0 4), and (0 0 6) reflections and presented on Fig. 5(b) for the sample S450a. For (0 0 2) and (0 0 4), a very sharp contribution is observed. Its breadth is limited by the instrumental resolution. A broad contribution is also observed and is enhanced for the samples S450a and S350 on weak reflections ((0 0 2) and (0 0 6)). This enhancement is interpreted as an increasing contribution of APD.<sup>24,26</sup> The enhancement of the APD contribution with the annealing is then interpreted in term of antiphase boundary instability.

For the sample S350, the lower  $T_g$  (350 °C) ensured a lower surface roughness as compared to  $T_g = 450$  °C (RMS measured from AFM images are, respectively, 1.2 nm and 2.6 nm) with, however, an APD contribution comparable to the annealed sample grown at 450 °C.

In a thorough analysis, the line profiles are fitted using a double component Pseudovoigt function in order to evaluate both the broad and thin contributions. Two main parameters are extracted from this and are reported in the Table I: (1) the quality factor (QF) which is the ratio of integrated intensity of the thin versus the broad contribution; (2) the integral

TABLE I. IB and QF are reported for the three samples and for the three different reflections. Correlations lengths (CL) and micro mosaic corresponding to the broad contributions are then extracted.

		S450	S450a	S350
		(450 °C)	(450 °C + Anneal)	(350 °C)
(0 0 2)	QF ( $A_T/A_B$ )	1.05	0.11	0.017
	IB ( $\text{nm}^{-1}$ )	0.045	0.0605	0.089
(0 0 4)	QF ( $A_T/A_B$ )	0.9	0.37	0.43
	IB ( $\text{nm}^{-1}$ )	0.52	0.041	0.104
(0 0 6)	QF ( $A_T/A_B$ )	0.5	0.08	0.026
	IB ( $\text{nm}^{-1}$ )	0.068	0.056	0.088
CL <sub>APR</sub> (nm)		24.5 ± 1	16.5 ± 1	11 ± 1
CL <sub>SR</sub> (nm)		24.5 ± 1	24.5 ± 2	9.5 ± 1
Mosaicity $\Delta M$		0.215 ± 0.01°	≤ 0.01°	0.22 ± 0.01°

breadth (IB) of the broad contribution. For the sample S450, high QF values for the three reflections reveal a low defect density. For the two other samples, lower QFs are observed for all reflections, but they are much lower on (0 0 2) and (0 0 6) APR reflections than on the (0 0 4) SR one, revealing the APD contribution. A Halder and Wagner parabolic approach<sup>28</sup> which is a variant of the Williamson-Hall plot method has been applied to these transverse scans.<sup>29–31</sup> This allows the separation of short range correlation length from micromosaicity in the broadening. Moreover, when QFs are much smaller on APR than on SR reflections, we can treat them separately and different correlation lengths can be given as shown in Table I.

### 3. Synchrotron XRD

Synchrotron XRD analysis has been performed on the sample S350. The H K L coordinates refer to the silicon substrate primitive cubic lattice. Fig. 6 presents RSM centred on (2 0 0) and (0 2 0) GaP reflections. Both RSM present 2 streaks going from the reflection along the directions parallel to [1 1 0] and [1  $\bar{1}$  0] axes. The streak oriented along [1 1 0] likely corresponds to the contributions of planar APD with APB lying on (1 1 0) and extended along the perpendicular direction. We call them (1 1 0) APD. Weaker streak extension along [1  $\bar{1}$  0] suggests weaker contribution of (1  $\bar{1}$  0) APD. A correlation length of 12 nm is found for [1 1 0] direction, in agreement with the value found on the lab setup (see Table I). A longer correlation length is found along [1  $\bar{1}$  0].

### 4. TEM analysis

Fig. 7 presents dark field TEM images. Fig. 7(a) shows a plan view, selecting the ( $\bar{2}$  0 0) reflection. In dark field imaging mode and for this layer thickness, dark lines correspond to APB. A high number of APB can be observed as thin dark lines in the picture. This suggests that most of these boundaries are parallel to the electron beam. Moreover, a preferential orientation of these dark line can be noticed along [1 1 0] and [1  $\bar{1}$  0] directions. We can also notice shorter APB to APB distances along [1 1 0] than along [1  $\bar{1}$  0]. Fig. 7(b) presents a [1  $\bar{1}$  0] zone axis cross-section dark field

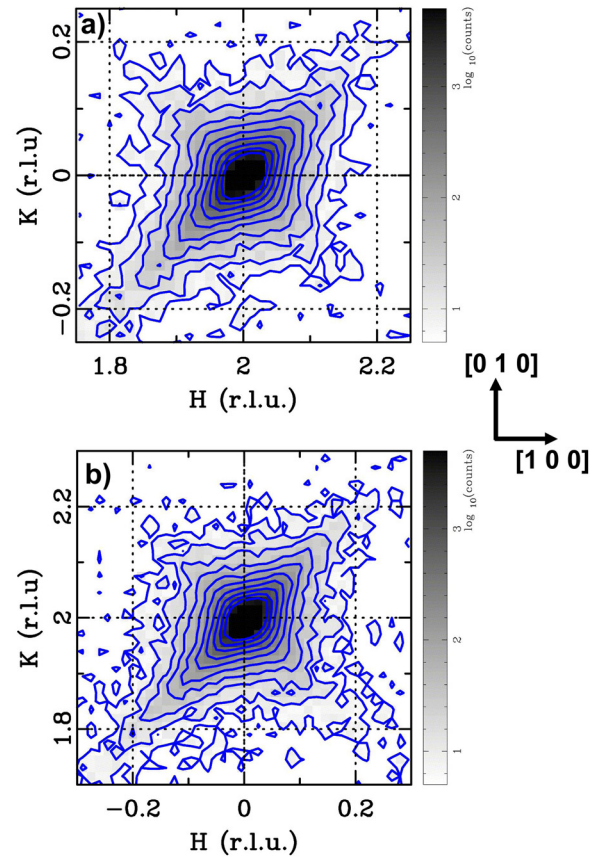


FIG. 6. RSM around the GaP (2 0 0) and (0 2 0) reflections showing diffuse streaks along the [1 1 0] and [1  $\bar{1}$  0] directions, characteristic of vertically oriented APD with (1 1 0) and (1  $\bar{1}$  0) APB (see text).

X-TEM image selecting the (1 1 1) reflection, which allows to detect APD in some particular excitation conditions.<sup>17</sup> Variations of contrasts associated to APD are effectively observed, with boundaries oriented close to (1 1 0) planes. These two dark field pictures confirm and complete what has been observed previously in synchrotron XRD measurements which concluded for the sample (S350) to the presence of high density APD with correlation lengths of the order of 11 nm along [1 1 0] and 17 nm along [1  $\bar{1}$  0]. This picture (Fig. 7(b)) also highlights the fact that most of these planar defects reach the active area, constituted here by the GaAsP QWs, which is detrimental for optical properties and may explain the evolution of time-resolved PL in part 2. Finally, the surface roughness of the sample seems to be correlated to the emerging anti-phase boundaries. This observation seems to confirm the modification of the growth equilibrium proposed in our recent work.<sup>27</sup> On this image, we can also observe others planar defects lying in the (1 1 1) planes such as MT and stacking fault (SF) (indicated by the arrows). The analysis of these defects will be reported in the following paragraph.

### D. Micro-twins and stacking faults analysis

Figures 8(a) and 8(b) present the RSM of the sample S350 around the ( $\bar{2}$  2 2) and ( $\bar{2}$   $\bar{2}$  2) GaP reflections and performed along the directions [1 1 0] and [0 0 1]. The RSM around ( $\bar{2}$  2 2) (Fig. 8(a)) is called hereafter “transverse”



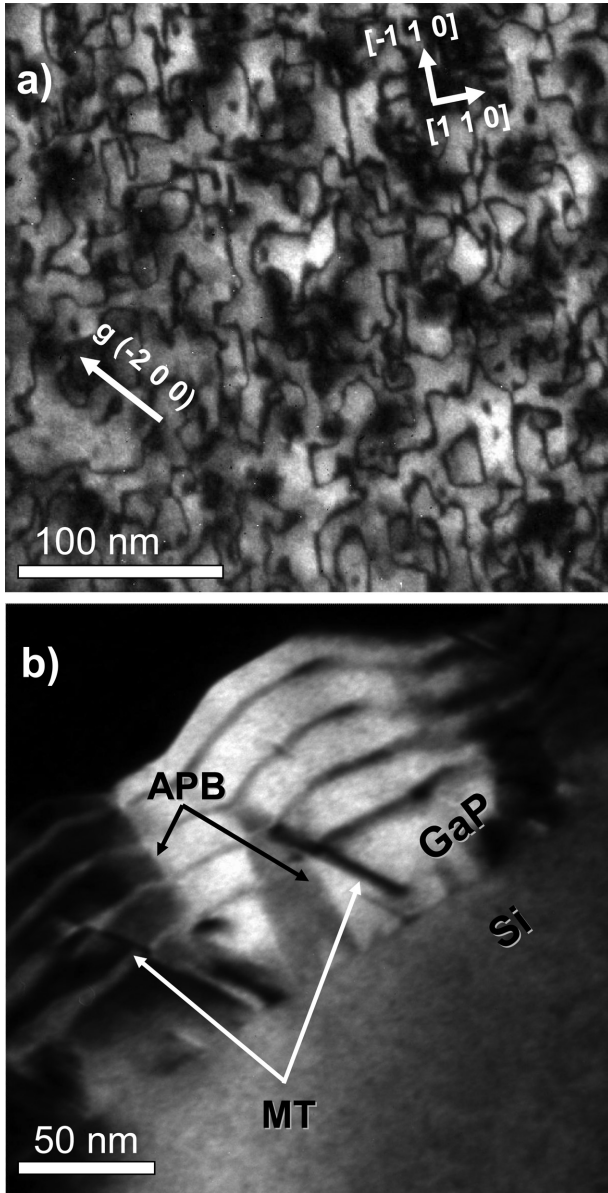


FIG. 7. (a) Plan view TEM  $(-2\ 0\ 0)$  dark field of 20 nm GaP/Si (S350) highlights APB; (b) cross sectional TEM  $(1\ 1\ 1)$  dark field image of GaAsP MQW/GaP/Si highlights planar defects in the  $(1\ 1\ 1)$  planes (MT and SF) but also APD. Many defects reach the active area.

because the  $[1\ 1\ 0]$  scanning direction is perpendicular to the scattering vector of the reflection and the RSM around  $(-2\ -2\ 2)$  (Fig. 8(b)) is called “longitudinal” because the scattering of the reflection is coplanar with the plane defined by the scanning directions. Two main features can be observed on these RSM: a broad contribution along the  $[1\ 1\ 0]$  direction and streaks elongated along the 3 fold axes directions ( $[1\ 1\ 1]$  and  $[1\ 1\ -1]$ ).

The transverse RSM (Fig. 8(a)) shows the presence of two streaks along  $[1\ 1\ -1]$  and  $[1\ 1\ 1]$  directions, while the longitudinal RSM (Fig. 8(b)) shows the presence of a streak along the  $[1\ 1\ 1]$  direction only. On this RSM, the absence of a visible streak along the  $[1\ 1\ -1]$  direction, rules out the SFs as the main contribution to the observed streaks. Indeed, SF lying along  $(1\ 1\ 1)$  planes induces a displacement of the lattice planes which is maximal and equal to  $1/3$  of the ZB

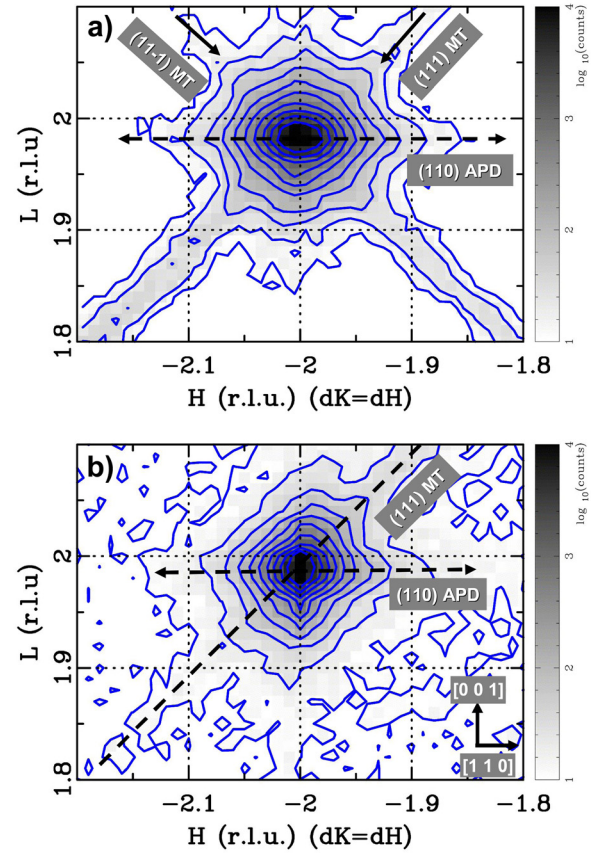


FIG. 8. Sample S350-RSM through  $(-2\ 2\ 2)$  and  $(-2\ -2\ 2)$  GaP reflections and along the  $[1\ 1\ 0]$  and  $[0\ 0\ 1]$  Si reciprocal space directions. The horizontal dashed arrows indicate the contribution of APD with  $(1\ 1\ 0)$  APB. The long dashed arrow (Fig. b) indicates the path of the scan shown on Fig. 9(a).

cell along the  $[1\ 1\ 1]$  direction across the SF boundary. This would induce the presence of a strong streak along the  $[1\ 1\ 1]$  direction around  $(1\ 1\ 1)$  reflections.

A complementary scan has been performed passing through GaP  $(-2\ -2\ 2)$  reflection centre along the  $[1\ 1\ 1]$  direction and shown on Fig. 9(a). Two additional peaks with lower intensities and very broad breadths are observed and can be attributed to extended planar MT. Hiruma *et al.*<sup>32</sup> have indeed characterized MT in InAs and GaAs whiskers grown on GaAs substrate by TEM. The TEM diffraction pattern showed new set of points, related by a  $180^\circ$  rotation to the main phase GaP reflections, with a  $[1\ 1\ 1]$  type rotation axis. Here, the two supplementary peaks observed in Fig. 9(a) correspond to one of the four possible MT variants. We call it the  $(1\ 1\ -1)$  variant because the MT boundaries are lying on  $(1\ 1\ -1)$  planes. The rotation axis lies along the  $[1\ 1\ -1]$  direction. The corresponding situation in reciprocal space is also given in Fig. 9(b) for this variant, and some of new MT reflections are reported. Coming back to the scan through MT reflections (Fig. 9(a)), we fit the peak  $(-1.66, -1.66, 2.33)$  and obtain an integral breath of the order of 0.15 (reciprocal lattice units). If we use this value as a correlation length characteristic of the average size of the MT along the  $[1\ 1\ 1]$  direction, this gives a value of about 2 nm. Moreover, two other scans performed through  $(-1.66, -1.66, 2.33)$  in the two perpendicular directions (not shown





## ACKNOWLEDGMENTS

We acknowledge M. Pasturel and V. Demange from Sciences Chimiques de Rennes for access to their XRD goniometer, M. I. Richard for a fruitful discussion about microtwins and stacking faults. We are also grateful to C. Gatel for geometrical phase analysis and C. Crestou for TEM samples thinning. This work is supported by the French national projects SINPHONIC (Grant No. 2011-JS03-006-01) and MENHIRS (Grant No. ANR-2011-PRGE-007-01).

- <sup>1</sup>S. F. Fang, K. Adomi, S. Iyer, H. Morkoc, H. Zabel, C. Choi, and N. Otsuka, *J. Appl. Phys.* **68**, R31 (1990).
- <sup>2</sup>T. Soga, T. Jimbo, and M. Umeno, *J. Cryst. Growth* **163**, 165 (1996).
- <sup>3</sup>K. Yamane, T. Kobayashi, Y. Furukawa, H. Okada, H. Yonezu, and A. Wakahara, *J. Cryst. Growth* **311**, 794 (2009).
- <sup>4</sup>Y. Takagi, Y. Furukawa, A. Wakahara, and H. Kan, *J. Appl. Phys.* **107**, 063506 (2010).
- <sup>5</sup>K. Yamane, T. Kawai, Y. Furukawa, H. Okada, and A. Wakahara, *J. Cryst. Growth* **312**, 2179 (2010).
- <sup>6</sup>B. Kunert, I. Németh, S. Reinhard, K. Volz, and W. Stolz, *Thin Solid Films* **517**, 140 (2008).
- <sup>7</sup>H. Yonezu, Y. Furukawa, and A. Wakahara, *J. Cryst. Growth* **310**, 4757 (2008).
- <sup>8</sup>W. Guo, A. Bondi, C. Cornet, H. Folliot, A. Létoublon, S. Boyer-Richard, N. Chevalier, M. Gicquel, B. Alshawa, A. L. Corre, J. Even, O. Durand, and S. Loualiche, *Phys. Status Solidi C* **6**, 2207 (2009).
- <sup>9</sup>K. Volz, A. Beyer, W. Witte, J. Ohlmann, I. Németh, B. Kunert, and W. Stolz, *J. Cryst. Growth* **315**, 37 (2011).
- <sup>10</sup>S. Liebich, M. Zimprich, A. Beyer, C. Lange, D. J. Franzbach, S. Chatterjee, N. Hossain, S. J. Sweeney, K. Volz, B. Kunert, and W. Stolz, *Appl. Phys. Lett.* **99**, 071109 (2011).
- <sup>11</sup>J. F. Geisz and D. J. Friedman, *Semicond. Sci. Technol.* **17**, 769 (2002).
- <sup>12</sup>O. Skibitzki, F. Hatami, Y. Yamamoto, P. Zaumseil, A. Trampert, M. A. Schubert, B. Tillack, W. T. Masselink, and T. Schroeder, *J. Appl. Phys.* **111**, 073515 (2012).
- <sup>13</sup>R. J. Potter and N. Balkan, *J. Phys.: Condens. Matter* **16**, S3387 (2004).
- <sup>14</sup>Y. González, L. González, and F. Briones, *J. Cryst. Growth* **111**, 120 (1991).
- <sup>15</sup>H. Döscher, O. Supplie, S. Brückner, T. Hannappel, A. Beyer, J. Ohlmann, and K. Volz, *J. Cryst. Growth* **315**, 16 (2011).
- <sup>16</sup>I. Németh, B. Kunert, W. Stolz, and K. Volz, *J. Cryst. Growth* **310**, 1595 (2008).
- <sup>17</sup>I. Németh, B. Kunert, W. Stolz, and K. Volz, *J. Cryst. Growth* **310**, 4763 (2008).
- <sup>18</sup>Y. Takagi, H. Yonezu, K. Samonji, T. Tsuji, and N. Ohshima, *J. Cryst. Growth* **187**, 42 (1998).
- <sup>19</sup>H. Kroemer, *J. Cryst. Growth* **81**, 193 (1987).
- <sup>20</sup>R. M. Sieg, S. A. Ringel, S. M. Ting, E. A. Fitzgerald, and R. N. Sacks, *J. Electron. Mater.* **27**, 900 (1998).
- <sup>21</sup>C. Cornet, C. Robert, T. Nguyen Thanh, W. Guo, A. Bondi, G. Elias, A. Létoublon, S. Richard, J.-P. Burin, M. Perrin, J.-M. Jancu, O. Durand, J. Even, S. Loualiche, H. Folliot, N. Bertru, A. Ponchet, and A. Le Corre, in *Compound Semiconductor Week (CSW/IPRM), 2011 and 23rd International Conference on Indium Phosphide and Related Materials* (IEEE, 2011), pp. 1–4.
- <sup>22</sup>A. Erol, editor, *Dilute III-V Nitride Semiconductors and Material Systems: Physics and Technology*, 1st ed. (Springer, 2008).
- <sup>23</sup>L. Kirste, K. M. Pavlov, S. T. Mudie, V. I. Punegov, and N. Herres, *J. Appl. Cryst.* **38**, 183 (2005).
- <sup>24</sup>D. A. Neumann, H. Zabel, R. Fischer, and H. Morkoc, *J. Appl. Phys.* **61**, 1023 (1987).
- <sup>25</sup>V. K. Dixit, T. Ganguli, T. K. Sharma, S. D. Singh, R. Kumar, S. Porwal, P. Tiwari, A. Ingale, and S. M. Oak, *J. Cryst. Growth* **310**, 3428 (2008).
- <sup>26</sup>A. Létoublon, W. Guo, C. Cornet, A. Boulle, M. Véron, A. Bondi, O. Durand, T. Rohel, O. Dehaese, N. Chevalier, N. Bertru, and A. Le Corre, *J. Cryst. Growth* **323**, 409 (2011).
- <sup>27</sup>W. Guo, A. Bondi, C. Cornet, A. Létoublon, O. Durand, T. Rohel, S. Boyer-Richard, N. Bertru, S. Loualiche, J. Even, and A. Le Corre, *Appl. Surf. Sci.* **258**, 2808 (2012).
- <sup>28</sup>N. C. Halder and C. N. J. Wagner, *Acta Crystallogr.* **20**, 312 (1966).
- <sup>29</sup>O. Durand, A. Létoublon, D. J. Rogers, and F. Hosseini Teherani, *Thin Solid Films* **519**, 6369 (2011).
- <sup>30</sup>O. Durand, A. Létoublon, D. J. Rogers, F. H. Teherani, C. Cornet, and A. Le Corre, *Proc. SPIE* **7940**, 79400L–79400L–14 (2011).
- <sup>31</sup>H. Jussila, S. Nagarajan, T. Huhtio, H. Lipsanen, T. O. Tuomi, and M. Sopanen, *J. Appl. Phys.* **111**, 043518 (2012).
- <sup>32</sup>K. Hiruma, M. Yazawa, T. Katsuyama, K. Ogawa, K. Haraguchi, M. Koguchi, and H. Kakibayashi, *J. Appl. Phys.* **77**, 447 (1995).
- <sup>33</sup>M. J. Hÿtch, E. Snoeck, and R. Kilaas, *Ultramicroscopy* **74**, 131 (1998).
- <sup>34</sup>T. J. Grassman, M. R. Brenner, S. Rajagopalan, R. Unocic, R. Dehoff, M. Mills, H. Fraser, and S. A. Ringel, *Appl. Phys. Lett.* **94**, 232106 (2009).